Possible structural control on the 2011 eruption of Puyehue-Cordón Caulle Volcanic Complex (southern Chile) determined by InSAR, GPS and seismicity

6 authors, including:

Andres Tassara
University of Concepción
97 PUBLICATIONS   **1,852** CITATIONS

Juan Baez
University of Chile
49 PUBLICATIONS   **679** CITATIONS

Daniel Basualto
Temuco Catholic University
24 PUBLICATIONS   **121** CITATIONS

Luis Lara
El Servicio Nacional de Geología y Minería
111 PUBLICATIONS   **1,616** CITATIONS

Some of the authors of this publication are also working on these related projects:

Monitoreo Humedales (co investigador) View project

times and mechanisms associated with the uplift of the broken foreland system of central patagonia View project

Possible structural control on the 2011 eruption of Puyehue-Cordón Caulle Volcanic Complex (southern Chile) determined by InSAR, GPS and seismicity

Anja Wendt,[1,*] Andrés Tassara,[2] Juan Carlos Báez,[3] Daniel Basualto,[4] Luis E. Lara[5] and Francisco García[2]

[1]*Bayerische Akademie der Wissenschaften, München, Germany. E-mail: wendt@keg.badw.de*
[2]*Departamento de Ciencias de la Tierra, Facultad de Ciencias Químicas, Universidad de Concepción, Chile*
[3]*Centro Sismológico Nacional, Universidad de Chile, Santiago, Chile*
[4]*Observatorio Volcanológico de los Andes del Sur, Servicio Nacional de Geología y Minería, Chile*
[5]*Red Nacional de Vigilancia Volcánica, Servicio Nacional de Geología y Minería, Chile*

SUMMARY

The Puyehue-Cordón Caulle Volcanic Complex (PCCVC) is one of the best examples of tectonic control on volcanism at the Southern Volcanic Zone of the Andes (southern Chile). The PCCVC comprises several volcanic centres that erupted dominantly SiO_2-rich magmas at the intersection of the trench-parallel Liquiñe-Ofqui Fault Zone (LOFZ) and an inherited NW–SE basement structure. The PCCVC began an explosive and later effusive eruption on 2011 June 4 causing decimetre- to metre-scale surface deformation that was observed by a series of Envisat ASAR satellite scenes. We modelled this data and complemented it with time-series of two continuous GPS stations and seismicity recorded by a local network. Deformation during the first 3 days of the eruption can be modelled either by two point sources aligned with the NW–SE Cordón Caulle graben or by a closing dyke with a significant component of left-lateral motion along the graben. These models are discussed with respect to their implications on the estimated rheology and the eruption mechanism. GPS observations near the volcanic complex reveal an additional, more localised effect related to the LOFZ in the south of the complex. Coeruptive deformation at the main geological structures of the PCCVC is further supported by relocated seismicity, which is concentrated along the Cordón Caulle graben and to the western side of the LOFZ.

Key words: Radar interferometry; Volcano seismology; Remote sensing of volcanoes; South America.

1 INTRODUCTION

Puyehue-Cordón Caulle Volcanic Complex (PCCVC, Fig. 1) is a long-lived active centre in the Southern Andes that has erupted basalts to rhyolites since the Middle Pleistocene (Lara *et al.* 2006; Singer *et al.* 2008). PCCVC is formed by three juxtaposed volcanoes (Cordillera Nevada caldera, Cordón Caulle fissure system and Puyehue stratovolcano) located to the NW of the intersection between a major trench-parallel fault system (the Liquiñe-Ofqui Fault Zone, LOFZ) with an old NW–SE basement structure (Cembrano & Lara 2009). The volcanoes were active coevally during an early stage but activity focused on Cordón Caulle and Puyehue since the

Late Pleistocene. Time-averaged eruptive rates (0.42 km³ kyr⁻¹) are one of the highest in the Southern Andes (Singer *et al.* 2008). The Holocene evolution is characterised by a remarkable emission of silica-rich magmas (∼70 per cent SiO_2) sourced at both Cordón Caulle and Puyehue (Lara *et al.* 2004). After a cone-destruction stage on Puyehue volcano at *ca.* 1.09 kyr, activity concentrated along Cordón Caulle system with a number of rhyodacitic domes and lava flows. Historical eruptions of 1921 and 1960 were sourced along the Cordón Caulle fissures with multiple vents (Lara *et al.* 2006). The 1960 event is thought to be a classic example of remote triggering caused by a nearby subduction earthquake, the giant M_w 9.5 Valdivia earthquake that occurred 36 hr before the eruption (Barrientos & Ward 1990; Lara *et al.* 2004).

The most recent eruption started explosively on 2011 June 4 after 2 months of shallow seismicity (Bertin *et al.* 2015). The phase of most intense explosive activity lasted for about 72 hr, when

---

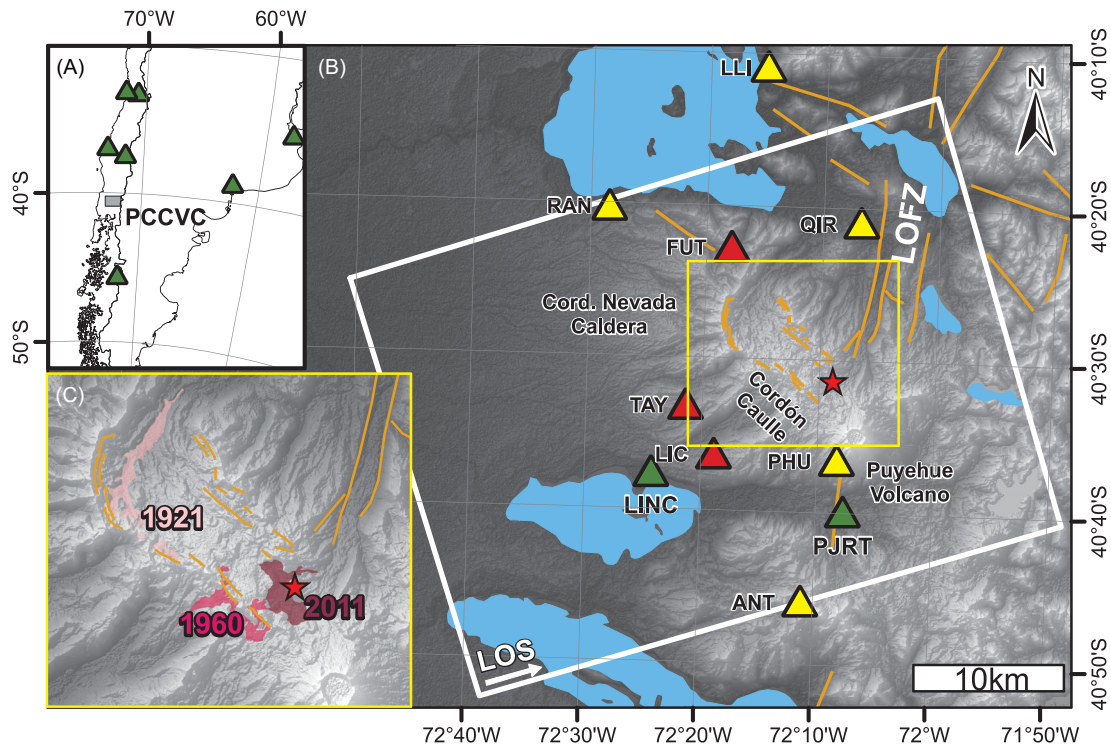* Formerly at: Centro de Estudios Científicos, Valdivia, Chile.

Figure 1. Tectonic setting of the Puyehue-Cordón Caulle Volcanic Complex (PCCVC). (a) Location of the study area in the Chilean Southern Andes. Green triangles show seven of the 16 GPS stations used in the GPS processing. (b) Digital elevation model of the SRTM-3, white rectangle marks the Envisat scene (white arrow labelled LOS indicates the line-of-sight direction), main faults and lineaments are mapped in orange, Liquiñe-Ofqui Fault Zone (LOFZ) extracted from the literature (e.g. Lara & Moreno, 2006), red star: the location of the vent activated during the June 2011 eruption, green triangles: continuous GPS stations installed days after the eruption, yellow and red triangles: seismic stations installed before and after the start of the eruption. The yellow box marks the extent of (c) Detail of the PCCVC showing the distribution of lava flows generated during the eruptions of 1921, 1960 (Lara *et al*. 2006) and 2011 (see e.g. Bertin *et al*. (2015) for a detailed analysis of lava emplacement). Note their coincidence with NW structures forming the walls of the Cordón Caulle graben.

ca. 0.96 km³ of tephra was erupted (0.75 km³ the first 2 d) as estimated by Pistolesi *et al*. (2015) based on a detailed stratigraphic analysis aided by satellite imagery. Considering the upper bound value of 750 kg m⁻³ for density of the juvenile fragments measured by these authors, the corresponding dry rock equivalent (DRE) volume of the tephra would be 0.27 km³.

After several days of waning intensity of the explosive phase, an effusive stage started on 15 June at very high rates that peaked near 70 m³ s⁻¹ a week later (Bertin *et al*. 2012; Tuffen *et al*. 2013). Effusion rates then gradually decreased over subsequent months and the eruption terminated between June and August 2012 with *ca*. 0.5 km³ of erupted lava (Bertin *et al*. 2012). Summing the DRE volume of the explosive phase and this volume of lava, the total erupted volume was *ca*. 0.77 km³.

Lava and tephra deposits of the eruption have been analysed to derive properties of the magma and its pre-eruption conditions (Castro *et al*. 2013; Jay *et al*. 2014; Alloway *et al*. 2015). Particularly, major and trace element analyses of Alloway *et al*. (2015) point to three distinct magma bodies contributing to the eruption, which these authors suggest could be structurally controlled by the complex spatial association between the NW-oriented PCCVC and the LOFZ. In addition, analytical and experimental petrologic results presented by Castro *et al*. (2013) suggest that the hybrid activity of the eruption (combining explosive and effusive phases) was likely fed by a dyke allowing simultaneous eruption of variably degassed magma patches.

A possible structural control on this eruption as inferred by these authors fits perfectly into the geological context of the PCCVC

and suggests that poorly studied but largely dangerous eruptions of viscous acidic magma could be more likely generated under such control. Indeed, the only other well-documented hybrid acidic eruption occurred in 2008 at Chaitén volcano in Southern Chile and was controlled by active structures of its basement as demonstrated by modelling surface deformation recorded by Interferometric Satellite Aperture Radar (InSAR) images (Wicks *et al*. 2011) and Global Positioning System (GPS) observations (Piña-Gauthier *et al*. 2013). However, similar studies on Cordón Caulle eruption 2011 (Bignami *et al*. 2014; Jay *et al*. 2014) did not consider an explicit control of crustal structures on co-eruptive surface deformation observed by InSAR, but used point sources embedded in an elastic medium (Mogi 1958) to model the deformation (Jay *et al*. 2014). In this contribution, we model SAR interferograms between February and December 2011 using Mogi point sources and alternative dyke-like sources in an elastic medium (Okada 1985), which we combine with continuous GPS data and locally recorded seismicity in order to evaluate the possible control exerted by the structural grain below PCCVC on the onset and evolution of its recent eruption.

2 PREVIOUS STUDIES ON SURFACE DEFORMATION AT PCCVC

Deformation patterns of volcanoes have been studied by InSAR in the phase of stress accumulation (e.g. Pritchard & Simons 2004a; Fournier *et al*. 2010 for the Southern Andes) as well as during eruptions (e.g. Froger *et al*. 2004; Biggs *et al*. 2010; Wicks *et al*.

Table 1. List of Envisat scenes over PCCVC used in this study. The table lists the dates of the two acquisitions, the name of the interferogram used in the text, the perpendicular baseline B_n and the height of ambiguity H_a.

Date1	Date2	Interferogram	B_n [m]	H_a [m]
2011-02-07	2011-03-09	2011-02/2011-03	45.7	335.3
2011-03-09	2011-04-08	2011-03/2011-04	230.0	66.6
2011-04-08	2011-05-08	2011-04/2011-05	− 240.8	− 63.6
2011-05-08	2011-06-07	2011-05/2011-06	− 98.4	− 155.7
2011-06-07	2011-07-07	2011-06/2011-07	153.2	100.0
2011-07-07	2011-10-05	2011-07/2011-10	− 265.2	− 61.1
2011-10-05	2011-12-04	2011-10/2011-12	150.7	108.2

2011). Previous InSAR-based studies for volcanoes of the Southern Volcanic Zone (SVZ) of the Andes recognised a notable surface deformation at PCCVC years before the 2011 eruption. Pritchard & Simons (2004a) using ERS data from 1996 and 1999 observed a subsidence equivalent to a rate of about 3 cm yr^{-1}, in a region coinciding with the NW-oriented Cordón Caulle graben at its intersection with the Cordillera Nevada Caldera. Fournier et al. (2010) observed inflation of the same region whose rate increased from about 1 cm yr^{-1} in 2003–2005 to almost 20 cm yr^{-1} in 2007–2008. This surface deformation signal was attributed to a volume increase of 0.06 km^3 distributed among 2 point sources at 7 and 4 km depth coinciding the first with the intersection of the graben with the caldera rim and the second at the centre of the graben near the 2011 eruptive vent. Pritchard et al. (2013) analysed the effect of the 2010 M_w 8.8 Maule earthquake on SVZ volcanoes finding coseismic subsidence at several volcanoes within 300 km of the epicentre. PCCVC is located at a distance of 500 km but showed an abnormal uplift signal of about 10 cm within a month of the earthquake. Previous InSAR analysis of the 2011 eruption has shown that it was accompanied by a large subsidence centred in the Cordillera Nevada caldera with a smaller peak west of Puyehue volcano just at the beginning of the eruption (Bignami et al. 2014; Jay et al. 2014). Jay et al. (2014) used point sources embedded in an elastic medium (Mogi 1958) to model the co-eruptive surface deformation as produced by in total three deflating sources at depths between 3 and 6 km, which are consistent with the depth range estimated for the pre-eruptive magma reservoir based on their petrological analysis. Two of these co-eruptive sources showed signs of inflation since 2007. Additionally, Jay et al. (2014) analysed the gas content of the erupted lava in order to estimate the compressibility of the magma, which is necessary to relate the modelled volume change the depth with the actually erupted volume.

3 DATA AND METHODS

3.1 InSAR processing

We analysed Envisat ASAR Image Mode data acquired between February and December 2011 (Table 1) that cover the months before and after the onset of the eruption. Scenes were recorded in ascending orbit in image swath IS6 with a high incidence angle of about 41°. Therefore, they exhibit less distortion of layover and foreshortening than data taken at steeper incidence angles. Since differential interferograms are sensitive to deformation, topography and atmospheric refraction, these effects have to be accounted for. While the effect of topography in the interferogram depends on the perpendicular baseline B_n between the acquisitions, deformation directly translates into interferometric phase scaled by the radar

wavelength. For Envisat ASAR data one fringe—a phase change of 2π—corresponds to 2.8 cm of deformation along the satellite line-of-sight direction (LOS).

Interferometric analysis of the Envisat data was done with the Gamma software (Werner et al. 2000). From each consecutive image pair, a differential interferogram with the shortest possible time span was computed (Fig. 2) omitting acquisitions from August and September that showed low coherence probably caused by wet snow cover. Differential interferograms were processed with 1×5 looks in range and azimuth direction, filtered by an adaptive filter based on the local fringe spectrum (Goldstein & Werner 1998) and masked using a coherence threshold. These interferograms form a time-series of consecutive time steps covering the months before and after the onset of the eruption. The topographic component of the interferometric phase was removed using the Digital Elevation Model SRTM-3 derived by the Shuttle Radar Topography Mission in 2000 (Farr et al. 2007). Perpendicular baselines range from 46 to 265 m (Table 1) resulting in different sensitivities to topography. Even for the interferograms with the largest baselines, the height of ambiguity H_a equivalent to a phase change of 2π in the interferogram amounts to about 60 m. The nominal accuracy of the SRTM topography is in the order of 6 m (Rodríguez et al. 2006), although higher errors can be expected in areas of high relief such as volcanoes. Converted into deformation this nominal height error corresponds to about 3 mm in LOS, which is a negligible fraction (<2 per cent) of the observed signal in the interferograms during the eruption. In contrast to the topographic contribution that can be corrected reliably, the effect of tropospheric refraction is more difficult to assess. Therefore, we use the available pre-eruption interferograms (Figs 2a–c) to estimate the magnitude of the tropospheric effect, although there could be more pronounced differences in atmospheric conditions than sampled in these three interferograms.

The resulting phase signal seen in interferograms 2011-02/2011-03 and 2011-03/2011-04 (Figs 2a and b) that is correlated with elevation is typical for a phase delay caused by the propagation through a layered atmosphere resulting in a differential signal between the base and the top of a topographic feature (e.g. Beauducel et al. 2000). At Llaima volcano also located in the Southern Volcanic Zone, Remy et al. (2015) observed a vertical phase gradient of up to 35 mm/1000 m related to precipitable water vapour. The twofold phase pattern of $\pm$ one fringe (2.8 cm in LOS) in the northern part of the April interferogram 2011-04/2011-05 (Fig. 2c), that was interpreted as deformational signal by Jay et al. (2014), is not correlated with topography and is thus more difficult to attribute unambiguously to either a tropospheric or deformational signal. In any case, it is neither clear subsidence nor uplift, and its amplitude does not exceed significantly the signal in the other pre-eruptive interferograms. The rms in these interferograms is indicative of the uncertainty caused by unmodelled effects. The rms values of
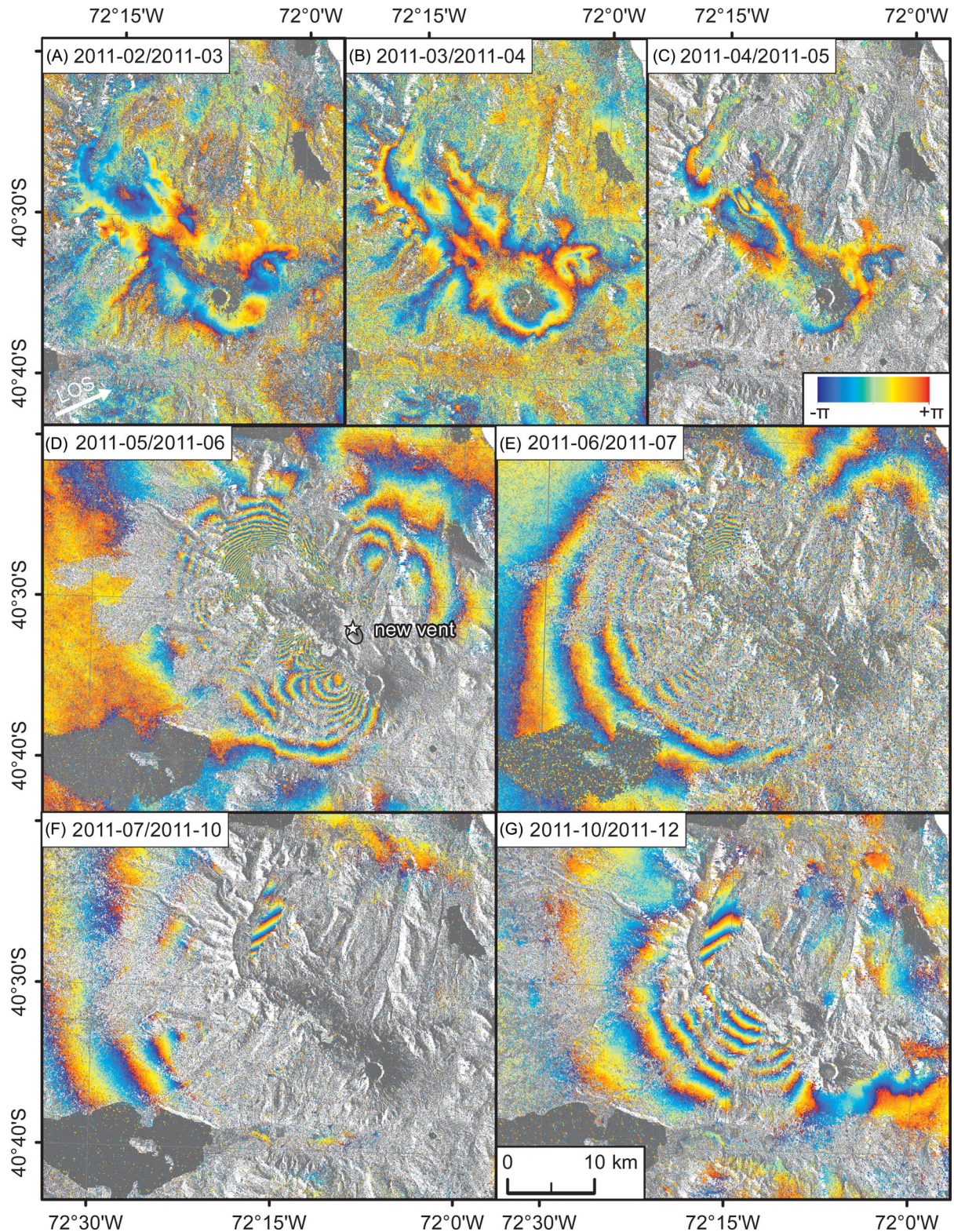
Figure 2. Envisat differential interferograms of PCCVC, upper row: pre-eruptive interferograms showing good coherence on the plateau and mainly tropospheric signal, middle row and lower row: co-eruptive interferograms all showing deflation of the edifice. The eruptive vent is marked by a star in (d) together with the outline of the ash plume that is only visible in the amplitude image acquired on 6 June.

0.40 fringes, 0.34 fringes and 0.76 fringes for 2011-02/2011-03, 2011-03/2011-04 and 2011-04/2011-05, respectively, convert to a deformational signal in LOS of 11, 10 and 21 mm, thus two orders of magnitude less than the signal observed in the interferogram 2011-05/2011-06 spanning the beginning of the eruption (Fig. 2d). The deformational signal in this interferogram with dense concentric fringes is clearly restricted to the volcanic complex, whereas the lowland in the west shows almost constant phase.

Interferograms after the start of the eruption show a considerable reduction in coherence with respect to pre-eruptive scenes. The densest part of the ash plume is faintly visible in the amplitude image taken 3 d after the start of the eruption (background of Fig. 2d, ash plume trace towards the SE of the new vent marked in black). Nevertheless, the incoherent part is considerably larger and stretches in the upwind direction, meaning that the ash plume is not solely responsible for decorrelation. The loss of coherence is rather attributed to the high fringe rate near the centre of the deformation in the interferogram spanning the onset of the eruption, additionally to the effect of changes in the ash deposits in all the interferograms. While phase unwrapping using the minimum cost flow method algorithm (Werner *et al*. 2003) did not pose any problems on pre-eruption interferograms, large phase gradients resulting in loss of coherence near the centre of deformation and fresh tephra deposits inhibited robust automatic phase unwrapping in the co-eruptive interferograms. Therefore, phase has been unwrapped by georeferencing fringes in order to avoid phase unwrapping errors and to downsample the data. This leads to an uneven distribution of data points, but the large incoherent areas have the same effect.

Each interferogram provides the projection of the 3-D deformation onto its line of sight (LOS). Ideally, data from ascending and descending tracks and different incidence angles are combined to resolve the three components of the displacement (Wright *et al*. 2004). In the case of PCCVC there are only Envisat data from an ascending orbit available, providing one projection of the 3-D deformation vector onto the LOS of the satellite (unit vector [−0.60, −0.26, 0.75] in east, north, up coordinates). Thus, the observed LOS displacement is less sensitive to movements in north–south direction.

The interferogram 2011-05/2011-06 (Fig. 2d) covers the first 3 d after the onset of the eruption on 4 June. It shows an increase in LOS distance (surface moves down and/or to the east) of up to 1.2 m collocated with the Cordillera Nevada caldera rim and a less prominent and less coherent LOS increase signal along the Cordón Caulle graben towards the eruptive vent. East of the graben, a decrease in LOS distance is observed, that is a deformation towards the satellite. The second eruptive interferogram 2011-06/2011-07 (Fig. 2e) shows an expansion of the deforming area towards the base of the complex with a more concentric distribution of fringes compared with the first co-eruptive interferogram and a less intense increase in LOS distance (up to 0.8 m at Cordillera Nevada caldera centre). The subsequent interferogram 2011-07/2011-10 covers a larger time span of 90 d because interferograms constructed using intermediate SAR scenes have significantly lower coherence due to snow cover and less deformation. Interferogram 2011-07/2011-10 has generally less coherence over the Cordón Caulle plateau and shows a concentric pattern of small-amplitude LOS increase, similar to the one observed in interferogram 2011-10/2011-12 covering 60 d until beginning of December 2011. The lower magnitude of deformation in these two interferograms makes them more susceptible to tropospheric effects that could contaminate the deformational signal.

3.2 Continuous GPS data

On 12 June, a few days after the start of the eruption, a preexisting campaign GPS site marked in bedrock (LINC, see Fig. 1) was re-occupied with a dual-frequency continuously recording GPS receiver (CGPS). After another 6 d, the CGPS site PJRT was installed in a stable zone of soil and marked by a steel monument similar to the shallow drilled braced monument of UNAVCO (http://kb. unavco.org/kb/article/shallow-drilled-braced-monumentoverview-301.html) to exclude monument instabilities. The data of these two sites were processed within a continental GPS network consisting of 16 IGS stations using the Bernese GPS Software V5.0 (Dach *et al*. 2007) applying precise orbit and Earth rotation parameters from IGS final products (Dow *et al*. 2009). More details about our processing strategy can be found in Bedford *et al*. (2013). For the datum definition of the GPS network we use the minimum constraint approach, applying the No Net Rotation and No Net Translation conditions for a group of selected reference stations, and therefore our results are compatible with ITRF2008 (Altamimi *et al*. 2011). The coordinates are reduced to a South American fixed frame, using a selected number of tectonically stable stations, which are located in the craton of the continent. Because the 2010 Maule earthquake occurred only 15 months earlier, the whole region was still subject to postseismic deformation. Due to the distance of more than 200 km between the southern limit of the Maule rupture zone and PCCVC, both the effects of afterslip and viscoelastic relaxation are considerably attenuated (Klein *et al*. 2016). Measured as well as modelled post-seismic deformation in the region were steadily decreasing throughout the second year after the earthquake and ranged as low as 10 to 20 mm yr^{-1} horizontally and less than 6 mm yr^{-1} vertically in the region of PCCVC (Klein *et al*. 2016), that is well below the observed signal.

3.3 Seismicity

Before 2010, the seismic network of the Observatorio Volcanológico de los Andes del Sur (OVDAS, Southern Andes Volcano Observatory belonging to SERNAGEOMIN, the Chilean Geological Survey) around PCCVC was composed by only two vertical short period stations (RAN and LLI in Fig. 1). These stations showed a significant increment of the seismic activity (swarms with Local Magnitude ML = 4.0) between June 2007 and January 2008, in coincidence with the notable shallow deformation evidenced by InSAR (Fournier *et al*. 2010; Jay *et al*. 2014). During the next three years (February 2008–January 2011), the seismic activity decreased and focused in the Cordillera Nevada caldera. After the 2010 Maule earthquake, three new broadband seismic stations (30 s) were installed around the volcano (QIR, PHU, ANT, Fig. 1) and previous short period stations were replaced by broadband instruments. After the eruption, three additional stations were installed (TAY, FUT, LIC) to complete a network of eight broadband stations around the complex.

The categorization of the seismic activity was made using the classification proposed by Lahr *et al*. (1994) and Chouet (2003), classifying about 14 000 earthquakes in 2011. From this database, around 1500 events were initially located with 47 per cent recorded between 16 April and the day of the eruption. The recorded seismicity was relocated using VELEST (Kissling 1988; Kissling *et al*. 1994) in order to improve the 1-D velocity model and establishing the corresponding delay times at each station via simultaneous mode Joint-Hypocentre-Determination (JHD). Details of data, methods and results regarding the seismicity before and during the eruption will be presented in another paper (Basualto *et al*., in preparation). Table 2 shows the obtained velocities for compressional and shear waves Vp and Vs as a function of depth representing the final velocity model. Finally, the JHD procedure generated a seismicity catalogue

Table 2. Seismic velocity model resulting after seismicity relocation process. The table shows values of *Vp* and *Vs* with depth.

Depth [km]	*Vp* [km s^{-1}]	*Vs* [km s^{-1}]
0.5	4.9	2.75
1.5	5.05	2.84
2.5	5.1	2.87
3.5	5.15	2.89
4.5	6.05	3.4
5.5	6.38	3.58
6.5	6.46	3.63
7.5	6.47	3.63
8.5	6.5	3.65

of 425 high quality events (more than eight seismic phases; gap stations locations <180°) divided in two different periods, before (174 events) and after (251 events) the start of the eruption. The final data solutions have a rms <0.15 and horizontal and vertical errors less than 0.65 km.

4 MODELLING SOURCES OF CO-ERUPTIVE SURFACE DEFORMATION OBSERVED BY InSAR

In order to assess the sources of the deformation pattern observed in the InSAR interferograms, analytical models were applied to relate subsurface volume change and displacements to surface deformation. To invert the first interferogram covering the onset of the eruption, 2 point sources (Mogi 1958) aligned approximately with the local maxima of deformation were assumed. For both sources, the exact centre coordinates and the parameters source depth and volume change were solved for iteratively. To derive the best-fitting parameters, the parameter space was searched for by uniform random sampling (Sambridge & Mosegaard 2002) to find the model that minimises the misfit represented by the rms of the differences between model and data at the sampled points. The resulting horizontal position (Fig. 3a) is located to the east of the maximum deformation recorded in the interferogram, because this maximum is the sum of vertical deformation (maximum above the source) and horizontal one (towards the source, relevant mainly east–west with opposite maxima on either side of the source) projected onto LOS. The region of positive LOS displacement east of the northern source is also a result of the horizontal displacement towards the source and does not reflect uplift as could be erroneously assumed if only vertical deformation were considered. Best fit was achieved for a deflating northern source below Cordillera Nevada caldera with a volumetric change of −0.096 km^3 at a depth of 3400 m and a second one below the intersection of the graben with the LOFZ near Puyehue volcano with a deflation of −0.017 km^3 at a depth of 3900 m (Table 3, Fig. 3a). The rms value between data and model amounts to 0.054 m, and the model accounts for 87 per cent of the total signal rms. However, as the deformation is proportional to volume change and inversely proportional to source depth, there is a trade-off between the two parameters (e.g. Pritchard & Simons 2004b), meaning that a smaller and shallower source can produce a similar deformation pattern as a larger, but deeper one. Additionally, the availability of only one projection of the 3-D deformation onto the look direction of one satellite path does not allow separating be-

tween horizontal and vertical displacement. The polar orbit with an almost NS flight direction results in a low sensitivity to deformation in this direction.

Assessing a deformation in an elastic half-space and thus neglecting the presence of topography affects the derived source parameters (Cayol & Cornet 1998), but the influence at PCCVC is less severe than at a typical axisymmetric stratovolcano because the slopes are less pronounced. As stated in Cayol & Cornet (1998), depth values have to be considered depth below the plateau level of 1500 m. Our modelled Mogi sources are similar in both spatial location and amplitude compared with those reported by Jay *et al.* (2014).

In order to evaluate the possibility of a structural control on eruption onset and considering that the eruptive vent is located along the Cordón Caulle graben to the southeast of the deforming region below Cordillera Nevada caldera, we also test a closing (deflating) dyke structure oriented NW-SE along the graben assuming in this case the analytical approximations of Okada (1985). In comparison with the Mogi model, more parameters have to be adjusted for the Okada model, that the geometry of the fault (central position, length, depth and width, strike orientation), direction of slip in terms of dip and rake, slip magnitude in the rake direction and opening perpendicular to the fault plane. We fixed geometric parameters following the geological structure of the graben (e.g. Sepúlveda *et al.* 2005; Lara *et al.* 2006; García 2015) and in consistency with seismicity presented below. The remaining free parameters were modelled searching for the minimum misfit with a Monte-Carlo method. Different tests especially for the dip of the dyke were performed, because the dip of the walls of the graben is supposed to decrease with increasing depth forming a trough (Sepúlveda *et al.* 2005; García 2015).

The best result was obtained for a combination of closing of a dyke-like structure and oblique left-lateral normal movement along the walls of this dyke (Table 3, Fig. 3b), a model with an rms of 0.082 m. Additional tests were done to evaluate two extreme cases with only closing or only slip along the dyke, both giving a worse fit. Without a slipping component, the inversion results in a deep (7400 m) horizontal sill with a closing of 5 m and an rms of 0.183 m. The second test precludes any component transverse to the dyke and thus any volume change, and therefore cannot explain the transfer of magma to the eruptive vent. This setting would result in a deeper dyke than the combined model with a slip of about 9 m and an rms of 0.086 m. The performance of the preferred model of combined slip and closing is slightly weaker than for the Mogi sources and accounts for 76 per cent of the total signal rms. Taking the amount of closure and the dimensions of the dyke into account, the change in volume is −0.062 km^3, about half of the one predicted by the Mogi sources.

As an additional exercise, we combined the dyke with the southern Mogi source to compensate for the large residuals there. The rms of the combined model is 0.072 m. The bulge of LOS increase in the south cannot be completely offset by the Mogi source, but the fit between data and model is considerably improved. The total volume change at depth is −0.078 km^3 for this combined scenario.

Deformation observed for the second co-eruptive interferogram 2011-06/2011-07 covering the waning stage of the explosive phase and the initiation of the effusive phase (Fig. 2e) was modelled with a single point Mogi source (Fig. 4) estimating a volume change of −0.169 km^3 at a depth of 5200 m. The rms between data and model amounts to 0.022 m and explains 94 per cent of the signal rms.
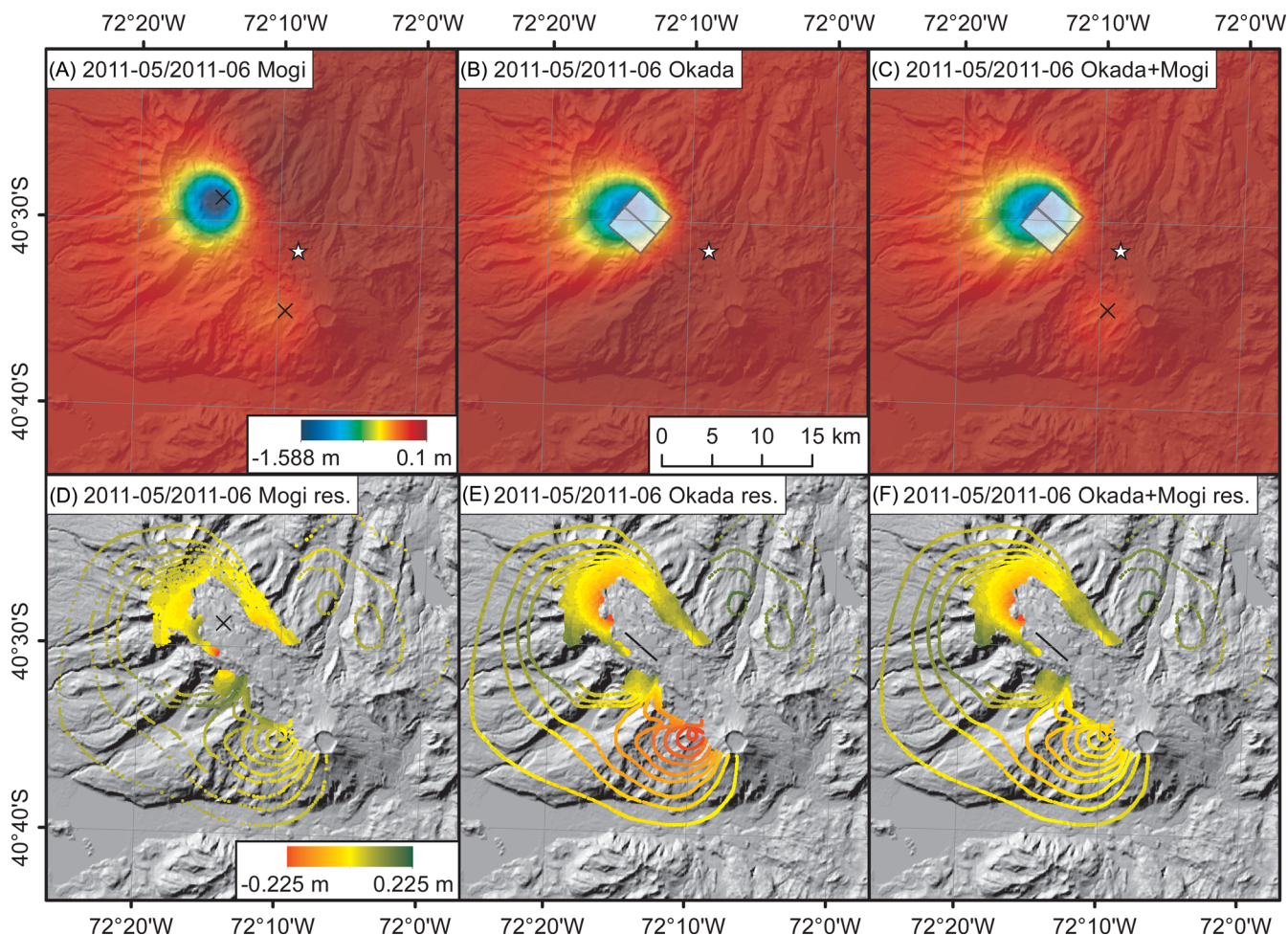
Figure 3. Different models for the interferogram in Fig. 2(d). Upper row: modelled LOS displacement, lower row: residuals. Scales in (a) and (d) refer to all subfigures in the respective rows; source centres are marked by crosses. Black line in (b), (c), (e) and (f) shows the trace of the centre line of the dyke with the grey plane depicting its extent. The eruptive vent is marked by a star.

Interferograms 2011-07/2011-10 (90 d), and 2011-10/2011-12 (60 d), were also modelled by single Mogi sources. The best-fit model of the former one has an rms of 0.008 m accounting for 87 per cent of the signal rms, while the latter results in an rms of 0.011 m explaining 85 per cent. While Jay *et al.* (2014) assume a common source location for all interferograms after 7 June, source location is adjusted for each interferogram independently in our approach. Although the source seems to move successively deeper and slightly towards the new vent, this should be interpreted with caution because of the tropospheric contamination that is more pronounced in these interferograms with smaller deformation. The estimated volume change rates are considerably smaller than in the first month of eruption. In general, our volume estimates agree with the ones of Jay *et al.* (2014) within about 25 per cent.

5 GPS-DERIVED DEFORMATION

Time-series of displacement for the two GPS sites situated in the south and southwest of the volcanic complex (Fig. 5) start during the second co-eruptive interferogram (2011-06/2011-07). During this time window both sites show a rapid displacement of 51 mm towards northeast in the case of LINC and of 19 mm to the north in the case

of PJRT. The vertical component, although more noisy, shows a notable subsidence with values on the order of 20 mm in LINC and about 200 mm in PJRT. This phase of rapid subsidence abruptly declined near 2011-07-07 coinciding with the day when the scene forming the interferograms 2011-06/2011-07 and 2011-07/2011-10 was taken by the satellite. The surface deformation recorded by both CGPS stations afterwards (between July and December 2011) maintains its azimuthal direction at lower rates. While PJRT remains vertically stable for the rest of the observed period, LINC shows a clear uplift starting in August, amounting to a net uplift of several centimetres compared to the beginning of the observations.

To compare the GPS displacement with InSAR-derived source models we first calculated a linear trend for the three components (N, E, U) of the time-series at both CGPS stations (Fig. 5) for the time spans of the particular InSAR scenes and then we projected the 3-D deformation along the LOS of the SAR satellite. A direct comparison of GPS deformation and InSAR data would otherwise be restricted to LINC because PJRT is surrounded by forest and does not show a coherent signal in the interferograms.

Therefore, we computed the predicted 3-D deformation at the position of both CGPS stations from the source models determined in section 4. Considering that the CGPS stations started data recording eight (LINC) and fourteen (PRJT) days after the initiation of

Table 3. Parameters of best-fitting models for the co-eruptive interferograms. For the Mogi models, location, depth and volume change were adjusted for. For the Okada model, fixed parameters are marked with an asterisk. The rms values after the adjustment are listed as well.

Interferogram 2011-05/2011-06, 30 d, Mogi models

Location (UTM 18S)	Depth [m]	Volume [km³]	rms [m]
734 500 m E, 5 515 300 m N	3400	−0.096	0.054
740 600 m E, 5 504 100 m N	3900	−0.017	

Interferogram 2011-05/2011-06, 30 d, Okada model

Location (UTM 18S)	Depth [m]	Length* [m]	Width* [m]	Strike* [°]	Dip [°]	Rake [°]	Slip [m]	Open [m]
735 000 m E, 5 513 000 m N	5500	4250	7250	139	42	−47	6.3	−2.0
		Volume [km³]	rms [m]					
		−0.062	0.082					

Interferogram 2011-05/2011-06, 30 d, Okada + Mogi model

Volume [km³]	rms [m]
−0.078	0.072

Interferogram 2011-06/2011-07, 30 d, Mogi model

Location (UTM 18S)	Depth [m]	Volume [km³]	rms [m]
736 100 m E, 5 514 200 m N	5200	−0.169	0.022

Interferogram 2011-07/2011-10, 90 d, Mogi model

Location (UTM 18S)	Depth [m]	Volume [km³]	rms [m]
736 800 m E, 5 512 500 m N	5700	−0.077	0.008

Interferogram 2011-10/2011-12, 60 d, Mogi model

Location (UTM 18S)	Depth [m]	Volume [km³]	rms [m]
738 250 m E, 5 513 100 m N	6200	−0.047	0.011
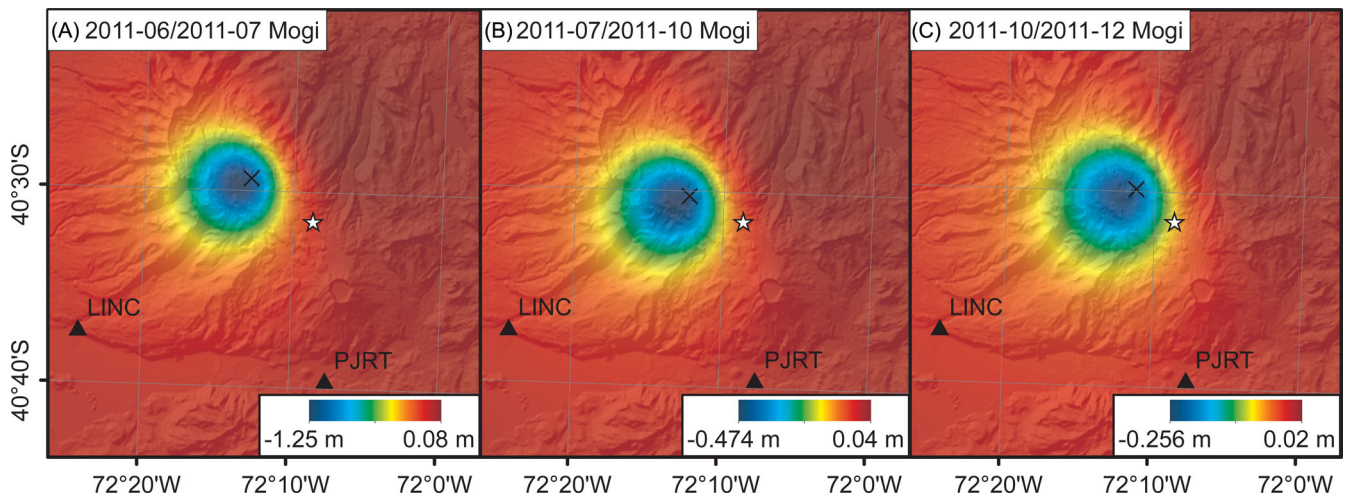
Figure 4. Model of LOS deformation in interferograms in Fig. 2(e), (f) and (g). Black cross marks the location of the respective Mogi source, black triangles indicate GPS sites, note different colour scales. The eruptive vent is marked by a star.

the eruption, the recorded deformation cannot be compared with the predictions of the source models derived from interferogram 2011-05/2011-06. Results of the comparison between measured and modelled displacements for the subsequent interferograms are listed in Table 4.

As expected, the modelled horizontal displacements point towards the centre of deformation (Fig. 6). The observed GPS vectors differ from this direction by 6° for LINC and by 23° for PJRT. For interferogram 2011-06/2011-07, displacements measured at LINC agree with those computed from the Mogi source model within uncertainties. For the station PJRT horizontal movement derived by GPS for the time of interferogram 2011-06/2011-07 is of smaller magnitude than the modelled one. On the contrary, measured subsi-

dence is one order of magnitude larger than predicted by the model. Unfortunately, this large deformation cannot be verified by InSAR directly because of the low coherence in this area, but the difference between model and observation is well above the error bound of the GPS measurements. The residual displacement at PJRT comparing the observation with the model prediction is 0.06 m in SE direction and a subsidence of 0.18 m. Any monument instability or local effect can be excluded, because the station has a steel monumentation as it is conventionally used for CGPS sites and is installed in a locally stable zone. However, this additional local effect could be related to the location of PJRT in the trace of the LOFZ pointing to a possible movement of the structure during the eruption.
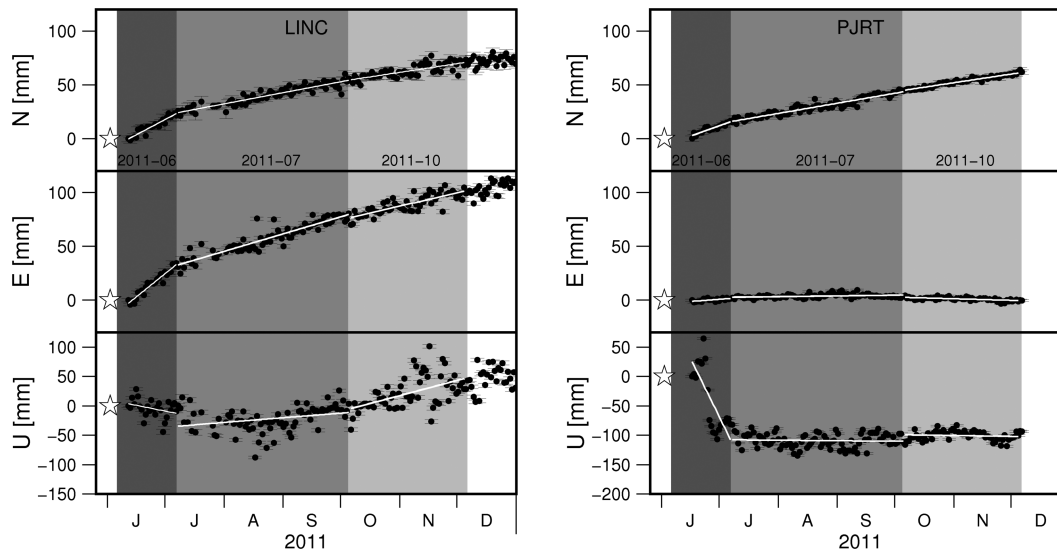
Figure 5. Time-series of daily solutions for northern (N), eastern (E) and vertical (U) component at continuous GPS stations LINC (left) and PJRT (right) starting 12 June and 18 June, respectively. Displacements are relative to the South American craton; for processing details see Section 3.2. Black dots are daily solutions with error bars, star marks the day of the eruption initiation (4 June). The time span of interferograms covering the time-series are highlighted in different grey levels and indicated at the bottom of the North panel; white lines depict linear trends for the time spans of the individual interferograms as listed in Table 4.

Table 4. Displacements (in m) both measured and modelled at GPS sites LINC and PJRT for the time span of the individual interferograms. For the LOS component uncertainties for both GPS and MOGI are given.

	LINC				PJRT			
	East	North	Up	LOS	East	North	Up	LOS
2011-06/2011-07 (30 d)								
GPS	0.043	0.028	−0.020	−0.048 ± 0.011	0.004	0.019	−0.200	−0.158 ± 0.030
Mogi	0.057	0.050	−0.017	−0.060 ± 0.020	−0.028	0.067	−0.016	−0.020 ± 0.020
2011-07/2011-10 (90 d)								
GPS	0.047	0.030	0.023	−0.019 ± 0.008	0.002	0.028	−0.003	−0.010 ± 0.004
Mogi	0.029	0.021	−0.010	−0.031 ± 0.020	−0.015	0.043	−0.014	−0.013 ± 0.020
2011-10/2011-12 (60 d)								
GPS	0.025	0.016	0.052	0.020 ± 0.010	−0.003	0.016	−0.003	−0.005 ± 0.003
Mogi	0.015	0.011	−0.005	−0.016 ± 0.020	−0.006	0.025	−0.008	−0.009 ± 0.020

In the case of interferograms 2011-07/2011-10 and 2011-10/2011-12, we note that the horizontal displacement observed at LINC is well reproduced by the prediction of the Mogi sources modelled from InSAR deformation. However, the uplift starting in August cannot be explained by a deflating Mogi source. While this disparity in the observed and modelled vertical displacement could point to the existence of rheological and/or geometrical complexity in the dynamics of the system that is not captured by the simple Mogi model, a non-tectonic seasonal signal cannot be excluded. Such seasonal vertical displacements are known from many GPS sites and are often related to atmospheric or local hydrological loading effects (e.g. Bevis *et al*. 2004; Tregoning & Watson 2009; Bos *et al*. 2010). Although the neighbouring PJRT station does not show a significant vertical movement in 2011after the pronounced initial subsidence in June, newer data of that site reveal seasonal height changes with a minimum in winter also typical for other stations in the region, but of smaller amplitude (Báez, personal communication). The deformation recorded by PJRT between July and September shows a northward displacement and no significant vertical movement, while the Mogi model predicts a larger movement

towards NNW and subsidence comparable to that at LINC. The horizontal residual amounts to 0.028 m towards SE. For the last time period (interferogram 2011-10/2011-12) GPS-derived deformation at PRJT and the prediction of the Mogi model coincide in direction with a slightly less pronounced deformation measured than modelled.

6 COMPARING MODELLED SOURCES WITH SEISMICITY

The seismic network recorded first signs of seismic unrest from February to April 2011, consisting in sporadic but significant (ML 2 to 4.3) Volcano-Tectonic (VT) and some Very Long Period (VLP) events located around the Cordillera Nevada caldera and the NW part of Cordón Caulle graben. During the next month, magnitude and frequency of seismicity gradually increased and expanded to the whole Cordón Caulle graben inside its bounding structures (Fig. 7a, NW-SE lineament). Few days before the eruption, the seismicity rapidly increased in magnitude and frequency and concentrated near the surface. At this stage, earthquakes were characterised by
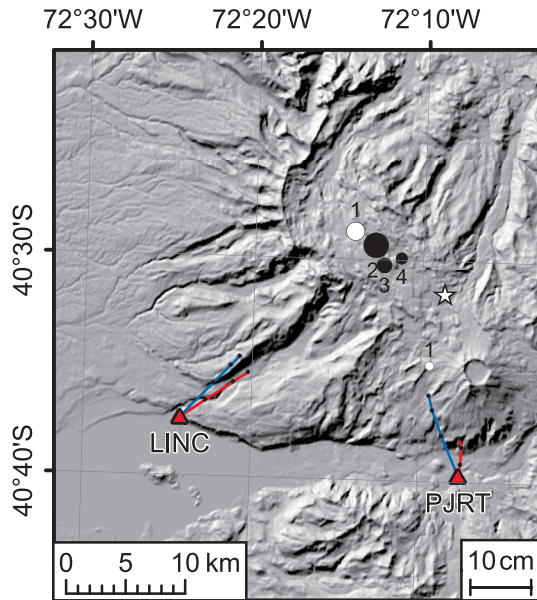
Figure 6. Map view of the GPS derived displacement vectors in red and the modelled vectors in blue. Mogi sources derived from the InSAR data that correspond to the deformation steps are depicted as black circles (2–4) and scaled in accordance to their volume change; the first Mogi sources not covered by GPS observations are drawn in white for completeness. The eruptive vent is marked by a star.

a blend of VT, hybrid (HB), and VLP sources. Similar seismicity with a mixture of different types were for instance recorded a few days before the eruption of Mount St. Helens (Qamar *et al.* 1983; Main 1987) and Augustine Volcano (Jacobs & McNutt 2011) and has been associated with the movement and/or ascent of magmatic fluids. Events were located along the NE wall of the Cordón Caulle graben at shallow depths and in a NE-SW oriented branch in the south (Fig. 7a, southern blue dots), suggesting the participation of another structure in the last phase, possibly related to an unmapped secondary branch to the LOFZ.

Fig. 7(b) shows the hypocentres recorded after the onset of the eruption (5 June – 20 July) indicating a more heterogeneous dis-

tribution of VT events along the graben with depths dominantly shallower than 5 km and a rapid decay of seismicity rate with time. Few events were actually recorded by the network after July (black dots in Fig. 7b) and they mostly concentrated at the western flank of Puyehue volcano likely along the reactivated branch of the LOFZ.

The notable concentration of seismicity along the Cordón Caulle graben and the western side of the LOFZ in the days immediately before and after the eruption strongly suggests that both structures could have experienced differential motion during the preparation phase of the eruption and in its subsequent development. This is also consistent with the location of the new active vent near the intersection of both structures.

7 DISCUSSION

The structural setting in which PCCVC is emplaced, at the intersection of the trench-parallel LOFZ with an old NW-SE inherited tectonic lineament, makes it a first-order example of a volcanic complex that has been constructed under a strong structural control (e.g. Sepúlveda *et al.* 2005; Lara *et al.* 2006; Singer *et al.* 2008; Cembrano & Lara 2009). Particularly, Cembrano & Lara (2009) note that the acidic composition of PCCVC during the Holocene indicates the presence of a long-lived reservoir where magma have sufficient time to differentiate because NW-oriented structures forming the walls of the reservoir are dominantly compressive under a dextral motion of the LOFZ. At shorter time-scales, a structural control was also apparent during 20th century fissure eruptions, particularly for the 1960 event that was likely triggered by the unclamping of the NW-oriented faults along the Cordón Caulle graben following the M_w 9.5 Valdivia earthquake (Lara *et al.* 2004; Bonali *et al.* 2013). For the case of the recent 2011 eruption, petrological analyses of erupted material allow inferring a possible tectonic control in the storage and co-eruptive interconnection of different melt pockets feeding the eruption (Alloway *et al.* 2015), and in the transport of variably-degassed magma through a dyke connecting the main reservoir with the eruptive vent (Castro *et al.* 2013). The fact that co-eruptive deflating point sources modelled by us and Jay *et al.* (2014) are several kilometres apart from this vent and collocated with it along the Cordón Caulle graben can be considered indirect
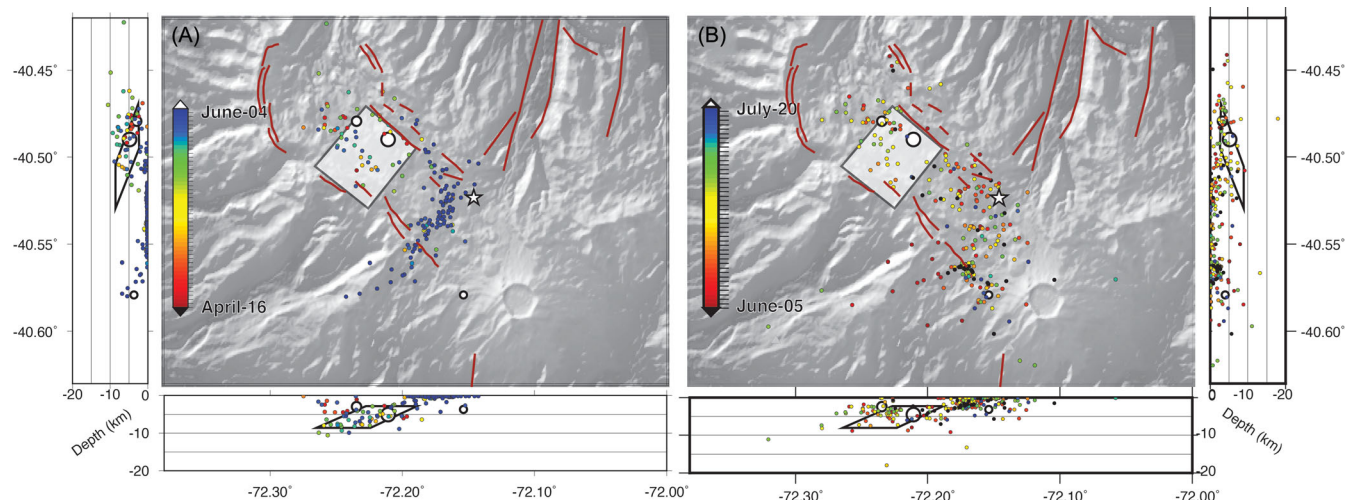

Figure 7. Relocation of seismicity. (a) Recorded from 16 April to 4 June (eruption start), (b) recorded from 5 June to 27 November 2011. The colours represent the temporal distribution of seismicity (black points in right panel are events recorded after 20 July). The red lines show the most important structures on the PCCVC. The white star represents the 2011 vent eruption. White circles mark positions of the Mogi sources with their size approximately proportional to the volume change, the Okada dyke is indicated as grey rectangle.

evidence of the activity of such a dyke. In following paragraph, we will discuss our results seeking for a more direct evaluation of a hypothetical structural control on this eruption.

Interferogram 2011-05/2011-06 (Fig. 2d), although only spanning the first 3 d of the eruption, depicts a surface subsidence of more than a meter associated with a volume change at depth of 0.11 km^3 when modelled with two Mogi point sources. The largest of these sources (accounting for approx. 85 per cent of the estimated volume change) is located near Cordillera Nevada caldera. This source roughly coincides with the main location of the inflating sources recognised by Fournier *et al.* (2010) and Jay *et al.* (2014) for the years before the eruption. This suggests that the main magmatic reservoir was located here but magma and gases were mobilised along the northern branch of Cordón Caulle graben towards the SE near its intersection with the LOFZ where the vent was finally opened. This is consistent with the spatiotemporal evolution of seismicity just before and during the first explosive phase of the eruption, with a SE expansion and shallowing of quakes inside the graben from Cordillera Nevada towards the vent. The spatiotemporal evolution of seismicity during this early stage was recorded by few local seismic stations and therefore it does not allow interpreting a clear pattern of dyke propagation with a front of seismicity moving from the reservoir towards the vent. Such a spreading effect has been observed for other well-studied cases such as the 1983 dyke intrusion in Kilauea (e.g. Rubin *et al.* 1998), the Dabbahu dyke propagation episode in Ethiopia (e.g. Grandin *et al.* 2011), or more recently, Bárdarbunga volcano in Iceland in 2014 when a dyke developed accompanied by propagating seismicity up to 45 km away from the deflating magma source (Sigmundsson *et al.* 2015).

Aiming to test the possible activity of a structure during the onset and first phase of the eruption, we intended an end-member model with respect to the point Mogi source supposing that surface deformation observed by InSAR near the intersection of Cordón Caulle graben with Cordillera Nevada in the NW was solely caused by a dyke-like Okada source. We note that such an end-member model is unrealistic in the sense that the assumed structure should mostly conduct magma to the surface from a proper (deflating) reservoir from where the magma is extracted, but the exercise helps evaluating the significance of the dyke-like hypothesis. The rms error between model prediction and observation is larger for a model combining this Okada source with a small Mogi source near Puyehue volcano in the SE (0.072 m) as compared with the two Mogi point sources model (0.054 m). However, the difference between the rms error of both models is nearly 2 per cent of the maximum LOS amplitude recorded by the first co-eruptive interferogram and therefore the two point Mogi sources model should be considered only slightly better than the combined dyke-like Okada + small Mogi source model.

Nevertheless, these alternative models substantially differ in the derived volume changes of the magmatic reservoir at depth (-0.113 km^3 vs -0.078 km^3). Comparing these predictions against observed erupted volumes could be useful for discussing the validity of both scenarios. For this exercise, we compare our calculated volume changes at depth (ΔV) for the first 3 d of the eruption (derived from interferogram 2011-05/2011-06) with an erupted volume (V_e) of 0.27 km^3 of DRE magma as estimated by Pistolesi *et al.* (2015) for this period. The ratio $V_e/\Delta V$ depends on the ratio between the compressibility of magma (K_m) and the compressibility of the elastic media surrounding the magmatic reservoir (K_r) (e.g. Mastin *et al.* 2009);

$$\frac{V_e}{\Delta V} = -\left(1 + \frac{K_m}{K_r}\right).$$ (1)

The compressibility of magma for the case of the 2011 eruption of PCCVC was estimated by Jay *et al.* (2014) based on fluid content of the erupted lava to $2.1 \pm 0.4 \times 10^{-10}$ Pa^{-1}. Given these values, equation 1 predicts that K_r should be $1.5 \pm 0.4 \times 10^{-10}$ Pa^{-1} if all the erupted magma was extracted from the two point deflating sources. The combined model of the closing dyke in the NW with the small deflating point source in the SE predicts $K_r = 8.5 \pm 4 \times 10^{-11}$ Pa^{-1}. We can use the seismic velocity model generated during relocation of seismicity (Table 2) with the relationship of Birch (1960) for calculating K_r as the inverse of bulk modulus B;

$$\frac{1}{K_r} = B = \rho\left(V_p^2 - \frac{4}{3}V_s^2\right).$$ (2)

For a density $\rho = 2550 \pm 150$ kg m^{-3} in the shallow upper crust, the compressibility derived from the seismic model at the depth range of the modelled sources (2.5–6.5 km) is of the order of $2 \pm 0.1 \times 10^{-11}$ Pa^{-1}. Both source models overestimate the value of compressibility derived from the seismic structure of the crust, although the value estimated by the dyke+point model is closer to the seismic estimation as a consequence of the lower volume change at depth that is needed because part of the surface deformation is related to the slip of the dyke. Alternatively, the difference between the small seismically-estimated compressibility and the higher value estimated from the source models could be explained by a strain weakening process decreasing the bulk modulus during the deformation associated with the eruption as proposed elsewhere (e.g. Gudmundsson 2004), although quantifying this effect is unclear.

As we can see, the two Mogi sources model generates a (slightly) better reproduction of InSAR-observed deformation than the combined NW Okada + SE Mogi model, but the later requires a smaller volume change at depth which is more consistent with the volume expected from equation 1 assuming a value of rock compressibility derived from the seismic velocity model. We therefore envisage an intermediate model for the NW deformation source: a deflating Mogi source at depth with a volume change of the order of -0.03 ± 0.01 km^3 (as required by equation 1 using the value of K_r derived from the seismic velocity model) from which magma is extracted and simultaneously conducted to the surface along a slipping dyke. Testing such a complex configuration is beyond the scope of our work but could be done in the future using a finite element approach considering the layered elastic properties implied by the seismic velocity model, and a point-like deflating source coupled with a slipping dyke.

Our Okada model predicts a left-lateral strike-slip movement of the SW-dipping dyke with a large normal component accounting for a total slip of 6.3 m of the hanging wall towards the SE at a depth between 2000 m and 9000 m. Given the dimensions of the dyke (Table 3) and a value of 20 GPa for the shear modulus G (as derived from the seismic velocity model using the relationship of Birch (1960) $G = \rho Vs^2$), this slip implies a seismic moment of 3.88×10^{18} Nm and a moment magnitude $M_w = 6.3$. From the 425 high quality events contained in our seismicity catalogue roughly half of them occurred inside the time window of the first co-eruptive interferogram. These events with local magnitudes between 0.3 and 4.9 released a total seismic moment of 1.85×10^{17} Nm, which correspond to a cumulated moment magnitude of 5.4. The National Earthquake Information Center PDE catalogue (http://earthquake.usgs.gov/earthquakes/search/) reports 22 quakes occurring during the corresponding time interval with magnitudes ranging between 3.6 and 5. The total seismic moment accounted by these quakes is 2.35×10^{17} Nm with an equivalent summed magnitude $M_w = 5.5$, very similar to the one computed

with our seismicity catalogue. This exercise shows that probably a small part of the slip resulting from the dyke-like model could be related with seismic energy released as the dyke propagated rupturing the walls of Cordón Caulle graben, with most of the motion being likely aseismic. Such discrepancy between slip and the associated released seismic moment is frequently observed during magmatic events (Pedersen *et al*. 2007).

Interferogram 2011-06/2011-07 (Fig. 2e), which covers the first weeks of the effusive phase of the eruption, shows deformation over a wider area but with smaller surface amplitude. The modelled Mogi source is located closer to the vent compared with the main point source of the earlier interferogram, but at an increased depth and producing a larger volume change at depth of 0.169 km^3. The erupted volume during the time of this interferogram comprises lava that was emitted starting 15 June after a phase of relative quiescence. Until 7 July (day of the second scene forming this interferogram), 0.10 km^3 of lava was accumulated (Bertin *et al*. 2012), a value lower than the computed volume change at depth. This inconsistency could be caused by two reasons, or a combination thereof: On the one hand, the erupted volume could be underestimated and a significant volume of ash and gases were evacuated between 6 June and 15 June, as it is actually shown by Bignami *et al*. (2014). On the other hand, the volume change at depth could be overestimated because of the simplified assumptions of the Mogi approximation with respect to the more complex elastic structure of the media implied by the seismic velocity model as discussed for the first interferogram.

To assess the role of the dyke during the effusive phase and to test whether analogously to the first interferogram a slipping dyke would produce a smaller volume and therefore a better agreement with the erupted volume, a similar dyke geometry was tested for the second co-eruptive interferogram. However, the solution tends towards a deep horizontal fault (depth > 7500 m) with only a small slip (1.9 m) but a large closing component, corresponding to a volume change at least comparable to the Mogi source. Therefore, the NW tending graben structure seems not to be active in this phase of the eruption.

After all these considerations the large SSE and downward residual motion of GPS site PJRT located near the main arm of the LOFZ still cannot be explained by the Mogi source. Together with the simultaneous concentration of seismicity along the graben and near the LOFZ (Fig. 7), this could indicate some local effect related to the activity of these structures.

The deformation rates recorded after mid-July 2011 are rather small compared with the first month of the eruption. Our continuous GPS observations actually indicate that rates of horizontal movement strongly decrease and surface subsidence stopped near 7 July, which is the day when the SAR scene forming interferograms 2011-06/2011-07 and 2011-07/2011-10 was obtained by the satellite. The deformation signal observed at interferograms 2011-07/2011-10 and 2011-10/2011-12 can be modelled as single Mogi sources with smaller volume change (-0.077 and -0.047 km^3, respectively) at monthly rates of the order of -0.025 km^3 per month. For the same time periods, Bertin *et al*. (2015) estimated an erupted lava volume of 0.18 km^3 for interferogram 2011-07/2011-10 and 0.13 km^3 for interferogram 2011-10/2011-12. Using equation 1 with the same magma compressibility as for the previous exercises, gives values of K_r of 1.57×10^{-10} and 1.19×10^{-10} Pa^{-1}. These values are similar to the one computed for the first co-eruptive interferogram based on the two Mogi sources and therefore one order of magnitude higher than the rock compressibility estimated by the seismic velocity model. The consistent difference between values of K_r derived from the Mogi source models for the first and last inter-

ferograms and the one estimated from the seismic velocity model is likely indicative of a systematic overestimation of volume changes at depths related to the complex rheologic structure of PCCVC not reflected by the simple isotropic linear elastic solid assumed by the Mogi approximation. As a corollary, this consistency also suggests that a missing erupted volume is likely needed to explain the large volume change at depth modelled for the second co-eruptive interferogram.

Since the effusion rates steadily decreased from mid-July onwards (Bertin *et al*. 2015), it can be suggested that the small surface deformation afterwards is not solely due to the further evacuation of magma from a deep reservoir but also related to the relaxation of the system after the eruption. This post-eruptive process could include a number of phenomena acting simultaneously [viscous and poroelastic relaxation of the upper crust, e.g. Plattner *et al*. (2013), Segall (2010), Froger *et al*. (2016), creeping at faults, e.g. Hill & Prejean (2007), densification of erupted lava flow and consequent increase of vertical loading, e.g. Lu *et al*. (2005), Odbert *et al*. (2015), etc.] that cannot be simulated by the simple elastic half-space model assumed by the point Mogi source.

8 CONCLUSIONS

We can conclude that a structural control on the 2011 PCCVC eruption, although being very likely from geological, volcanological and petrological perspectives, is only indirectly shown by data and results presented and discussed here. Particularly, InSAR-observed surface deformation associated with the first explosive phase of the eruption can be better explained by a model considering two point Mogi sources aligned with the Cordón Caulle graben than a combined model of a closing and slipping Okada dyke in the NW with a small Mogi point in the SE. However, the model including the slipping dyke requires a much smaller volume change at depth, which translates into a smaller implied value of rock compressibility that is more consistent with the value derived from the local seismic velocity model generated during seismicity relocation. Thus, it seems very likely that a more complex source configuration at the intersection of Cordón Caulle graben with Cordillera Nevada could reconcile these observations. At least for the first, explosive phase of the eruption, we envisage a deflating point-like source at depth from which a smaller amount of magma and gases is extracted (compared with the estimated amount of the two point sources model) that is connected with a dyke propagating along the northern wall of Cordón Caulle graben towards its intersection with the LOFZ where the vent was finally opened. Seismicity accompanying this first phase was recorded by few local stations and it does not show a clear migration of a rupturing front as observed for other well-studied dyke propagating events. However, the spatiotemporal evolution of seismicity shows that quakes were concentrated below Cordillera Nevada until days before the eruption and then they show an expansion towards the SE and simultaneous shallowing. This is at least consistent with the idea of a pulse of magma and gases advancing from the main reservoir in the NW along the graben, opening the walls of the graben to create the vent at the intersection with the main LOFZ branch and finally stimulating the onset of the explosive phase. Since the seismic moment computed from the left-lateral motion of the dyke-like structure is an order of magnitude higher than the cumulated moment released by quakes recorded during the same period of time, we suggest that most of the slip that could have accompanied the dyke propagation was aseismic. After 3 d of volcanic paroxysm, the InSAR-observed surface deformation

recorded during the first weeks of the effusive phase is well modelled by an isolated deflating Mogi source near the source of the first phase, and an Okada dyke-like model can be discarded. This is expected because once the structural channel between magmatic reservoir and eruptive vent is created, magma and gases are just conducted along this channel with no need for further motion of the structure. However, the concentration of seismicity along the SE part of Cordón Caulle graben and the western branch of the LOFZ, in conjunction with large vertical and SSE residual motion (with respect to the InSAR-derived source model) observed at the continuous GPS station PJRT located near the main branch of the LOFZ, both suggest that the structural framework over which PCCVC is installed was partially activated also during the effusive phase.

This eruption is the first large acidic, explosive eruption that is relatively well monitored by local seismic and geodetic networks. These observations indirectly suggest that such an eruption could be at least partially controlled by the activation of structures forming the plumbing system of a long-lived magmatic reservoir, a control which was also inferred for the hybrid explosive-effusive rhyodacitic eruption of Chaitén volcano in 2008 (Wicks *et al.* 2011; Piña-Gauthier *et al.* 2013). A different modelling approach based on finite element methods could perhaps help in the future to test more complex rheology and source scenarios combining deformation and seismicity during the 2011 Cordón Caulle eruption that could more clearly show the structural control on this kind of largely dangerous eruptions.

REFERENCES

Alloway, B.V., Pearce, N.J.G., Villarosa, G., Outes, V. & Moreno, P.I., 2015. Multiple melt bodies fed the AD 2011 eruption of Puyehue-Cordón Caulle, Chile, *Sci. Rep.,* **5,** 17589.

Altamimi, Z., Collilieux, X. & Métivier, L., 2011. ITRF2008: an improvement solution of the international terrestrial reference frame, *J. Geod.,* **85,** 457–473.

Barrientos, S.E. & Ward, S.N., 1990. The 1960 Chile earthquake: inversion for slip distribution from surface deformation, *Geophys. J. Int.,* **103**(3), 589–598.

Beauducel, F., Briole, P. & Froger, J.-L., 2000. Volcano-wide fringes in ERS synthetic aperture radar interferograms of Etna (1992–1998): deformation or tropospheric effect?, *J. geophys. Res.,* **105**(B7), 16 391–16 402.

Bedford, J. *et al.*, 2013. A high-resolution, time-variable afterslip model for the 2010 Maule $M_w = 8.8$, Chile megathrust earthquake, *Earth planet. Sci. Lett.,* **383,** 26–36.

Bertin, D., Amigo, A., Lara, L.E., Orozco, G. & Silva, C., 2012. Erupción del Cordón Caulle 2011–2012: evolución de la fase efusiva, in *Congreso Geológico Chileno,* Vol. 13, pp. 545–547.

Bertin, D., Lara, L.E., Basualto, D., Amigo, Á., Cardona, C., Franco, L., Gil, F. & Lazo, J., 2015. High effusion rates of the Cordón Caulle 2011–2012 eruption (Southern Andes) and their relation with the quasi-harmonic tremor, *Geophys. Res. Lett.,* **42**(17), 7054–7063.

Bevis, M., Kendrick, E., Cser, A. & Smalley, R., 2004. Geodetic measurement of the local elastic response to the changing mass of water in Lago Laja, Chile, *Phys. Earth planet. Inter.,* **141**(2), 71–78.

Biggs, J., Mothes, P., Ruiz, M., Amelung, F., Dixon, T.H., Baker, S. & Hong, S.H., 2010. Stratovolcano growth by co-eruptive intrusion: the 2008 eruption of Tungurahua Ecuador, *Geophys. Res. Lett.,* **37**(21), L21302, doi:10.1029/2010GL044942.

Bignami, C., Corradini, S., Merucci, L., de Michele, M., Raucoules, D., De Astis, G., Stramondo, S. & Piedra, J., 2014. Multisensor satellite monitoring of the 2011 Puyehue-Cordon Caulle eruption, *IEEE J. Select. Top. Appl. Earth Observ. Remote Sens.,* **7**(7), 2786–2796.

Birch, F., 1960. The velocity of compressional waves in rocks to 10 kilobars: 1. *J. geophys. Res.,* **65**(4), 1083–1102.

Bonali, F.L., Tibaldi, A., Corazzato, C., Tormey, D.R. & Lara, L.E., 2013. Quantifying the effect of large earthquakes in promoting eruptions due to stress changes on magma pathway: the Chile case, *Tectonophysics,* **583,** 54–67.

Bos, M.S., Bastos, L. & Fernandes, R.M.S., 2010. The influence of seasonal signals on the estimation of the tectonic motion in short continuous GPS time-series, *J. Geodyn.,* **49**(3), 205–209.

Castro, J.M., Schipper, C.I., Mueller, S.P., Militzer, A.S., Amigo, A., Parejas, C.S. & Jacob, D., 2013. Storage and eruption of near-liquidus rhyolite magma at Cordón Caulle, Chile, *Bull. Volcanol.,* **75**(4), 1–17.

Cayol, V. & Cornet, F.H., 1998. Effects of topography on the interpretation of the deformation field of prominent volcanoes—application to Etna, *Geophys. Res. Lett.,* **25,** 1979–1982.

Cembrano, J. & Lara, L.E., 2009. The link between volcanism and tectonics in the southern volcanic zone of the Chilean Andes: a review, *Tectonophysics,* **471**(1), 96–113.

Chouet, B., 2003. Volcano Seismology, *Pure appl. Geophys.,* **160,** 739–788.

Dach, R., Hugentobler, U., Fridez, P. & Meindl, M., 2007. *Bernese GPS Software Version 5.0,* Astronomical Institute, University of Bern.

Dow, J.M., Neilan, R.E. & Rizos, C., 2009. The international GNSS service in a changing landscape of global navigation satellite systems, *J. Geod.,* **83,** 191–198.

Farr, T.G. *et al.*, 2007. The shuttle radar topography mission. *Rev. Geophys.,* **45**(2), RG2004, doi:10.1029/2005RG000183.

Fournier, T.J., Pritchard, M.E. & Riddick, S.N., 2010. Duration, magnitude, and frequency of subaerial volcano deformation events: new results from Latin America using InSAR and a global synthesis. *Geochem. Geophys. Geosyst.,* **11,** Q01003, doi:10.1029/2009GC002558.

Froger, J.L., Fukushima, Y., Briole, P., Staudacher, T., Souriot, T. & Villeneuve, N., 2004. The deformation field of the August 2003 eruption at Piton de la Fournaise, Reunion Island, mapped by ASAR interferometry, *Geophys. Res. Lett.,* **31**(14), L14601, doi:10.1029/2004GL020479.

Froger, J.L., Cayol, V. & Famin, V., 2016. The March–April 2007 eruptions of Piton de la Fournaise as recorded by interferometric data, in *Active Volcanoes of the Southwest Indian Ocean*, pp. 271–286, eds Bachelery, P., Lenat, J.-F., Di Muro, A. & Michon, M., Springer.

García, F., 2015. Modelo structural del complejo volcánico Puyehue-Cordón Caulle y análisis sísmico del control estructural durante la erupción del 2011, *PhD thesis,* Universidad de Concepción, Concepción, Chile.

Goldstein, R.M. & Werner, C.L., 1998. Radar interferogram filtering for geophysical applications, *Geophys. Res. Lett.,* **25**(21), 4035–4038.

Grandin, R. *et al.*, 2011. Seismicity during lateral dike propagation: Insights from new data in the recent Manda Hararo–Dabbahu rifting episode (Afar, Ethiopia), *Geochem. Geophys. Geosyst.,* **12**(4), Q0AB08, doi:10.1029/2010GC003434.

Gudmundsson, A., 2004. Effects of Young's modulus on fault displacement, *Comptes Rendus Geoscience,* **336**(1), 85–92.

Hill, D. & Prejean, S., 2007. *Dynamic Triggering, in Treatise on Geophysics*, pp. 258–288, ed. Kanamori, H., Elsevier.

Jacobs, K. & McNutt, S., 2011. Using seismic b-values to interpret seismicity rates and physical processes during the preeruptive earthquake swarm

at Augustine Volcano 2005–2006, in *The 2006 Eruption of Augustine Volcano, Alaska*, pp. 59–83, eds Power, J.A., Coombs, M.L. & Frey-mueller, J.T., U.S. Geological Survey Professional Paper 1769.

Jay, J., Costa, F., Pritchard, M., Lara, L.E., Singer, B. & Herrin, J., 2014. Locating magma reservoirs using InSAR and petrology before and during the 2011–2012 Cordón Caulle silicic eruption, *Earth planet. Sci. Lett.*, **395**, 254–266.

Kissling, E., 1988. Geotomography with local earthquake data, *Rev. Geophys.*, **26**, 659–698.

Kissling, E., Ellsworth, W.L., Eberhart-Phillips, D. & Kradolfer, U., 1994. Initial reference models in local earthquake tomography, *J. geophys. Res.*, **99**(B10), 19635–19646.

Klein, E., Fleitout, L., Vigny, C. & Garaud, J.D., 2016. Afterslip and viscoelastic relaxation model inferred from the large-scale post-seismic deformation following the 2010 M_w 8.8 Maule earthquake (Chile), *Geophys. J. Int.*, **205**(3), 1455–1472.

Lahr, J.C., Chouet, B., Stephens, C., Power, J. & Page, R., 1994. Earthquake classification, location, and error analysis in a volcanic environment: implications for the magmatic system of the 1989–1990 eruptions at Redoubt Volcano, Alaska, *J. Volc. Geotherm. Res.*, **62**, 137–151.

Lara, L.E. & Moreno, H., 2006. *Geología del Complejo Volcánico Puyehue-Cordón Caulle, X Región de Los Lagos,* Servicio Nacional de Geología y Minería, Carta Geológica de Chile, Serie Geología Básica, 1 mapa escala 1:50.000.

Lara, L.E., Naranjo, J.A. & Moreno, H., 2004. Rhyodacitic fissure eruption in Southern Andes (Cordón Caulle; 40.5°S) after the 1960 (M_w: 9.5) Chilean earthquake: a structural interpretation, *J. Volc. Geotherm. Res.*, **138**(1), 127–138.

Lara, L.E., Moreno, H., Naranjo, J.A., Matthews, S. & Pérez de Arce, C., 2006. Magmatic evolution of the Puyehue–Cordón Caulle volcanic complex (40 S), Southern Andean Volcanic Zone: from shield to unusual rhyolitic fissure volcanism, *J. Volc. Geotherm. Res.*, **157**(4), 343–366.

Lu, Z., Masterlark, T. & Dzurisin, D., 2005. Interferometric synthetic aperture radar study of Okmok volcano, Alaska, 1992–2003: magma supply dynamics and postemplacement lava flow deformation, *J. geophys. Res.*, **110**(B2), B02403, doi:10.1029/2004JB003148.

Main, I., 1987. A characteristic earthquake model of the seismicity preceding the eruption of Mount St. Helens on 18 May 1980, *Phys. Earth planet. Inter.*, **49**, 283–293.

Mastin, L.G., Lisowski, M., Roeloffs, E. & Beeler, N., 2009. Improved constraints on the estimated size and volatile content of the Mount St. Helens magma system from the 2004–2008 history of dome growth and deformation, *Geophys. Res. Lett.*, **36**(20), L20304, doi:10.1029/2009GL039863.

Mogi, K., 1958. Relations between the eruptions of various volcanoes and the deformations of the ground surfaces around them, *Bull. Earthq. Res. Inst.*, **36**, 99–134.

Odbert, H., Taisne, B. & Gottsmann, J., 2015. Deposit loading and its effect on co-eruptive volcano deformation, *Earth planet. Sci. Lett.*, **413**, 186–196.

Okada, Y., 1985. Surface deformation due to shear and tensile faults in a half-space, *Bull. seism. Soc. Am.*, **75**(4), 1135–1154.

Pedersen, R., Sigmundsson, F. & Einarsson, P., 2007. Controlling factors on earthquake swarms associated with magmatic intrusions; constraints from Iceland, *J. Volc. Geothermal Res.*, **162**, 73–80.

Piña-Gauthier, M., Lara, L.E., Bataille, K., Tassara, A. & Báez, J.C., 2013. Co-eruptive deformation and dome growth during the 2008–2009 Chaitén eruption, Southern Andes, *Andean Geol.*, **40**(2), 310–323.

Pistolesi, M. *et al.*, 2015. Complex dynamics of small-moderate volcanic events: the example of the 2011 rhyolitic Cordón Caulle eruption, Chile, *Bull. Volcanol.*, **77**(1), 1–24.

Plattner, C., Amelung, F., Baker, S., Govers, R. & Poland, M., 2013. The role of viscous magma mush spreading in volcanic flank motion at Kilauea Volcano, Hawai'i, *J. geophys. Res.*, **118**(5), 2474–2487.

Pritchard, M.E. & Simons, M., 2004a. An InSAR-based survey of volcanic deformation in the southern Andes, *Geophys. Res. Lett.*, **31**, L15610, doi:10.1029/2004GL020545.

Pritchard, M.E. & Simons, M., 2004b. An InSAR-based survey of volcanic deformation in the central Andes, *Geochem. Geophys. Geosyst.*, **5**, Q02002, doi:10.1029/2003GC000610.

Pritchard, M.E., Jay, J.A., Aron, F., Henderson, S.T. & Lara, L.E., 2013. Subsidence at southern Andes volcanoes induced by the 2010 Maule, Chile earthquake, *Nature Geosci.*, **6**(8), 632–636.

Qamar, A., St. Lawrence, W., Moore, J.N. & Kendrick, G., 1983. Seismic signals preceding the explosive eruption of Mount St. Helens, Washington, on 18 May 1980, *Bull. seism. Soc. Am.*, **73**, 1797–1813.

Remy, D., Chen, Y., Froger, J.L., Bonvalot, S., Cordoba, L. & Fustos, J., 2015. Revised interpretation of recent InSAR signals observed at Llaima volcano (Chile), *Geophys. Res. Lett.*, **42**(10), 3870–3879.

Rodríguez, E., Morris, C.S. & Belz, J.E., 2006. A Global Assessment of the SRTM Performance, *Photogram. Eng. Remote Sens.*, **72**(3), 249–260.

Rubin, A.M., Gillard, D. & Got, J.L., 1998. A reinterpretation of seismicity associated with the January 1983 dike intrusion at Kilauea Volcano, Hawaii, *J. geophys. Res.*, **103**(B5), 10 003–10 015.

Sambridge, M. & Mosegaard, K., 2002. Monte Carlo methods in geophysical inverse problems. *Rev. Geophys.*, **40**(3), 1009, doi:10.1029/2000RG00089.

Segall, P., 2010. *Earthquake and Volcano Deformation*. Princeton Univ. Press.

Sepúlveda, F., Lahsen, A., Bonvalot, S., Cembrano, J., Alvarado, A. & Letelier, P., 2005. Morpho-structural evolution of the Cordón Caulle geothermal region, Southern Volcanic Zone, Chile: Insights from gravity and $^{40}Ar/^{39}Ar$ dating, *J. Volc. Geotherm. Res.*, **148**(1), 165–189.

Sigmundsson, F. *et al.*, 2015. Segmented lateral dyke growth in a rifting event at Bárðarbunga volcanic system, Iceland, *Nature*, **517**, 191–195.

Singer, B.S., Jicha, B.R., Harper, M.A., Naranjo, J.A., Lara, L.E. & Moreno-Roa, H., 2008. Eruptive history, geochronology, and magmatic evolution of the Puyehue-Cordón Caulle volcanic complex, Chile, *Bull. geol. Soc. Am.*, **120**(5–6), 599–618.

Tregoning, P. & Watson, C., 2009. Atmospheric effects and spurious signals in GPS analyses, *J. geophys. Res.*, **114**, B09403, doi:10.1029/2009JB006344.

Tuffen, H., James, M.R., Castro, J.M. & Schipper, C.I., 2013. Exceptional mobility of an advancing rhyolitic obsidian flow at Cordón Caulle volcano in Chile, *Nature Commun.*, **4**, 2709, doi:10.1038/ncomms3709.

Werner, C., Wegmüller, U., Strozzi, T. & Wiesmann, A., 2000. Gamma SAR and interferometric processing software, in *Proceedings of the ERS-ENVISAT Symposium,* Gothenburg, Sweden, pp. 16–20.

Werner, C., Wegmüller, U., Strozzi, T. & Wiesmann, A., 2003. Processing strategies for phase unwrapping for INSAR applications, in *Proceedings EUSAR 2002,* Cologne, 4–6 June, 2002.

Wicks, C., de La Llera, J.C., Lara, L.E. & Lowenstern, J., 2011. The role of dyking and fault control in the rapid onset of eruption at Chaitén Volcano, Chile, *Nature*, **478**(7369), 374–377.

Wright, T.J., Parsons, B.E. & Lu, Z., 2004. Toward mapping surface deformation in three dimensions using InSAR, *Geophys. Res. Lett.*, **31**, L01607, doi:10.1029/2003GL018827.